Fundamental Research 4 (2024) 178–187

Contents lists available at ScienceDirect

Fundamental Research

journal homepage: http://www.keaipublishing.com/en/journals/fundamental-research/

Article

Tumor microenvironment-activated theranostic nanoreactor for NIR-II Photoacoustic imaging-guided tumor-specific photothermal therapy

Nan Yang [a], Hui Li [a], Changyu Cao [a], Lei Zhao [a], Xuejiao Song [a,*], Wenjun Wang [b], Wenjing Xu [c], Yewei Zhang [c,*], Peng Chen [d], Xiaochen Dong [a,*]

[a] Key Laboratory of Flexible Electronics (KLOFE) and Institute of Advanced Materials (IAM), School of Physical and Mathematical Sciences, Nanjing Tech University (NanjingTech), Nanjing 211816, China
[b] School of Physical Science and Information Technology, Liaocheng University, Liaocheng 252059, China
[c] Department of Hepatobiliary and Pancreatic Surgery, the Second Affiliated Hospital of Nanjing Medical University, Nanjing 210011, China
[d] School of Chemical and Biomedical Engineering, Lee Kong Chian School of Medicine, Nanyang Technological University, 62 Nanyang Drive, Singapore 637459, Singapore.

ARTICLE INFO

Article history:
Received 5 December 2021
Received in revised form 8 April 2022
Accepted 20 April 2022
Available online 15 May 2022

Keywords:
Nanoparticles
Photoacoustic imaging
Second near-infrared region
Tumor microenvironment
Self-sufficient H_2O_2

ABSTRACT

Theranostic agents that can be sensitively and specifically activated by the tumor microenvironment (TME) have recently attracted considerable attention. In this study, TME-activatable 3,3′,5,5′-tetramethylbenzidine (TMB)-copper peroxide (CuO_2)@poly(lactic-co-glycolic acid) (PLGA)@red blood cell membrane (RBCM) (TCPR) nanoparticles (NPs) for second near-infrared photoacoustic imaging-guided tumor-specific photothermal therapy were developed by co-loading CuO_2 NPs and TMB into PLGA camouflaged by RBCMs. As an efficient H_2O_2 supplier, once exposed to a proton-rich TME, CuO_2 NPs can generate H_2O_2 and Cu^{2+}, which are further reduced to Cu^+ by endogenous glutathione. Subsequently, the Cu^+-mediated Fenton-like reaction produces cytotoxic ·OH to kill the cancer cells and induce TMB-mediated photoacoustic and photothermal effects. Combined with the RBCM modification-prolonged blood circulation, TCPR NPs display excellent specificity and efficiency in suppressing tumor growth, paving the way for more accurate, safe, and efficient cancer theranostics.

1. Introduction

Theranostic nanoplatforms, which integrate diagnostic and therapeutic functions, have paved the way for cancer management to achieve the goal of personalized medicine, owing to their unique advantages, including engineerable functionalities, early detection of tumors, visualization of the spatiotemporal biodistribution of nanoagents, and real-time assessment of therapeutic effects [1–6]. Among various theranostic nanoplatforms, optical theranostic nanoagents have drawn increasing attention due to their minimal invasiveness, high specificity, and spatial-temporal selectivity.

Photothermal therapy (PTT), which causes cancer cell death by using incident light energy to induce hyperthermia using photothermal agents (PTAs), has substantial potential in oncotherapy. Compared to other diagnostic methods, photoacoustic imaging (PAI) has the advantages of excellent tissue penetrability and low scattering and dissipation in biological tissues; hence, PAI-based theranostic nanoplatforms have drawn increasing attention among all developed nanoplatforms. PAI/PTT theranostic nanoplatforms show great promise for tackling cancers.

Most of the reported theranostic agents lack tumor specificity, and the diagnostic signals and therapeutic effects are always in “on” mode. Intravenous (*i.v.*) injected nanoplatforms, which are prone to phagocytosis and retention by the reticuloendothelial system, not only lead to non-specific interference during cancer diagnosis, but also cause side effects during treatment. Therefore, it is preferable to design stimuli-responsive theranostic agents that can be exclusively activated in a specific focal area to overcome the aforementioned barriers.

Unlike normal tissues, the tumor microenvironment (TME) is generally characterized by hypoxia, acidosis, overexpressed H_2O_2, and high interstitial fluid pressure [7]. Taking advantage of these unique characteristics, TME-activatable theranostic agents (ATAs) have gained broad interest as the diagnostic and therapeutic features they induce can be “switched on” in tumors and “switched off” in normal tissues, which facilitates precise tumor detection and ablation with minimal non-specific damage. Such theranostic systems can be built by employing chemical reactions that are initiated exclusively at the tumor sites [8–15]. For instance, H_2O_2-activated agents provide a feasible choice for constructing TME-activated ATAs [16–21]. However, the H_2O_2 levels in the TME are

* Corresponding authors.
E-mail addresses: xjsong@njtech.edu.cn (X. Song), zhangyewei@njmu.edu.cn (Y. Zhang), iamxcdong@njtech.edu.cn (X. Dong).

https://doi.org/10.1016/j.fmre.2022.04.021

often insufficient for ATAs to realize efficient cancer theranostics, and integrating H_2O_2-activated ATAs with self-sufficient H_2O_2 could be an effective strategy to tackle this challenge.

PTT, which causes cancer cell death by using light energy to induce hyperthermia via PTAs, has substantial potential in oncotherapy owing to its minimal invasiveness and short treatment period [22]. Exploring PTAs with high photothermal conversion efficiency (PCE) and strong near-infrared (NIR) absorption, especially in the second near-infrared (NIR-II) band (1000–1350 nm), is critical for improving the antitumor efficacy of PTT [23–25]. Noble metal nanoparticles (NPs), metal chalcogen NPs, polyoxometalates, semiconducting polymers, and MXene nanomaterials are the most common NIR-II-absorbing materials [26–28]. Among these, organic PTAs based on NIR-II-absorbing p-conjugated semiconducting polymers have been used for PTT and PAI of deep-seated tumors owing to their high extinction coefficient, good biocompatibility, flexible structure, and engineerable physicochemical properties. Although the PCE of PTAs has dramatically improved in recent years, the side effects induced by strong hyperthermia on adjacent normal tissues cannot be ignored. Thus, there is an urgent need to develop novel PTAs with enhanced specificity and efficiency to improve the patient therapeutic outcomes, while reducing the potential side effects.

Copper peroxide (CuO_2) NPs, with a high H_2O_2 self-production capacity, and 3,3′,5,5′-tetramethylbenzidine (TMB), with excellent hydroxyl radical (·OH)-activated photothermal efficiency in the NIR-II region, were co-loaded into biodegradable poly(lactic-co-glycolic acid) (PLGA), which was subsequently coated with the red blood cell membrane (RBCM) of mice to fabricate TMB-CuO_2@PLGA@RBCM (TCPR) NPs for *in vivo* TME-activated theranostics (Scheme 1).

Specifically, TCPR NPs present various desirable properties: (1) With the aid of RBCMs, TCPR NPs can be efficiently accumulated in tumor locations due to the enhanced permeability and retention (EPR) effect. (2) The loaded CuO_2 in TCPR can generate H_2O_2 via the reaction between CuO_2 and protons in the mildly acidic TME to increase the concentration of H_2O_2 *in situ*. (3) The Fenton-like reaction mediated by Cu ions and H_2O_2 (both endogenous and supplied) can efficiently generate sufficient •OH to oxidize TMB for NIR-II PAI and PTT. The theranostic performance of the rationally designed nanosystem was investigated *in vitro* and *in vivo*.

2. Section of Experimentation

2.1. Materials

The Shanghai Xinbao Fine Chemical Factory supplied $CuCl_2{\cdot}2H_2O$. H_2O_2, CH_2Cl_2, NaOH, and PLGA were purchased from Nanjing Chemical Reagent Co. Ltd. Poly(vinylpyrrolidone) (PVP), polyvinyl alcohol (PVA), and TMB were obtained from Adamas-beta Co. Ltd.

2.2. Characterization

A scanning electron microscope (SEM, S4800; Hitachi, Japan) was used to characterize the morphology of the samples, and a Zetasizer Nano series (Nano ZS90; Malvern Instrument Ltd.) was used to characterize the hydrodynamic size distribution and zeta potential. Similarly, an ultraviolet (UV)–visible (Vis)–NIR spectrometer (UV-3600; Shimadzu, Japan) was used to measure the absorption spectrum, whereas inductively coupled plasma mass spectrometry (NeXion 300X) was used to measure the concentration of Cu. An infrared camera (FLIR) was used to capture the thermal pictures, and photoacoustic (PA) imaging was done using LOIS-3D (TomoWave Laboratories, USA). Flow cytometry (BD FACSCalibur) was used to detect the apoptotic rate of the cells, and biochemical analysis was performed using an automatic biochemical analyzer (Chemray 800; Leidu Life Technology, China). Lastly, an X-ray photoelectron spectroscopy (XPS) analysis was performed to further confirm the valence state of Cu.

2.3. Synthesis of CuO_2, TCP, and TCPR NPs

PVP (500 mg) was dissolved in a $CuCl_2{\cdot}2H_2O$ (1 mL, 0.05 M) solution, and NaOH (10 mL, 0.01 M) and H_2O_2 (100 L) were then added to the mixture, from which the CuO_2 NPs were obtained via ultrafiltration after 30 min of stirring.

PLGA (10 mg) was dissolved in 2 mL of CH_2Cl_2, and a mixture of 1% PVA (500 μL) and CuO_2 NP solution (200 mg mL^{-1}, 250 μL) was added. The microemulsion bubbles were formed twice using an ultrasonic cell grinder for 15 min, and TMB (5 mg mL^{-1}, 7 mL) in dimethyl sulfoxide (DMSO) was then mixed with the microemulsion. Finally, the prepared solution was progressively added to 6 mL of 2% PVA solution under ultrasonic pulverization for 10 min. The TMB-CuO_2@PLGA (TCP) NPs were collected via centrifugation after stirring overnight at 25 °C.

While RBCM was obtained from fresh blood of mice, hypotonic phosphoric acid buffer (1:50) was added to red blood cells (RBCs) and placed in the refrigerator overnight. The RBC solution was then purified via centrifugation (9000 rpm/min) to obtain pure RBCM, while the TCP NPs were stirred with RBCM for two hours to obtain TCPR NPs using the nanoprecipitation method.

2.4. Detection of H_2O_2

$KMnO_4$ (10 μg mL^{-1}) solution was treated with H_2O_2, phosphate-buffered saline (PBS), and TCPR NPs to detect the production of H_2O_2. Subsequently, UV–Vis–NIR spectra ranging from 400–1100 nm was measured. The presence of H_2O_2 was detected by the appearance and increase in the absorbance of oxTMB at 650 nm, which could also react with KI to generate I^{3-}, resulting in an absorbance peak at 350 nm. Finally, the H_2O_2 concentration was determined by plotting a standard curve.

2.5. Photothermal Effect

The FLIR thermal camera was used to measure the temperature curves of TCPR NPs, which were incubated for 8 h for TMB oxidization before measuring UV–Vis absorption spectra, with varying concentrations at various pH values under 1060 nm laser irradiation. Meanwhile, the temperature change associated with TCPR NP dispersion was also observed in a quartz tube under laser irradiation with various power intensities (1.0, 0.8, 0.6, 0.4, and 0.2 W cm^{-2}), and their optical stability (100 mg L^{-1}) under acidic conditions (pH 5.5) was also tested. The following equation was used to calculate the PCE (η):

$$\eta = h_S\left(T_{max} - T_{sur}\right) - Q_{Dis}/I(1 - 10^{-A1060}) \quad (1)$$

The symbol η denotes the PCE, while the cell surface area is denoted by “s” and the heat transfer coefficient is denoted by “h”. Similarly, the equilibrium temperature is T_{Max}, ambient temperature is T_{Sur}, and I is the incident laser power. When a quartz cell and water are irradiated with laser light, QDis is the baseline energy generated, and A_{1060} is the absorbance of the sample at 1060 nm. “hs” is calculated from substituting equations:

$$\tau = mc/h_S \quad (2)$$

The mass and capacity of pure water are “m” and “c,” respectively, and the following formula can be used to compute the time constant (τ):

$$t = -\tau ln\theta \quad (3)$$

$$\theta = \left(T - T_{Sur}\right)/\left(T_{Max} - T_{Sur}\right) \quad (4)$$

in which θ is the driving force temperature of the solution.

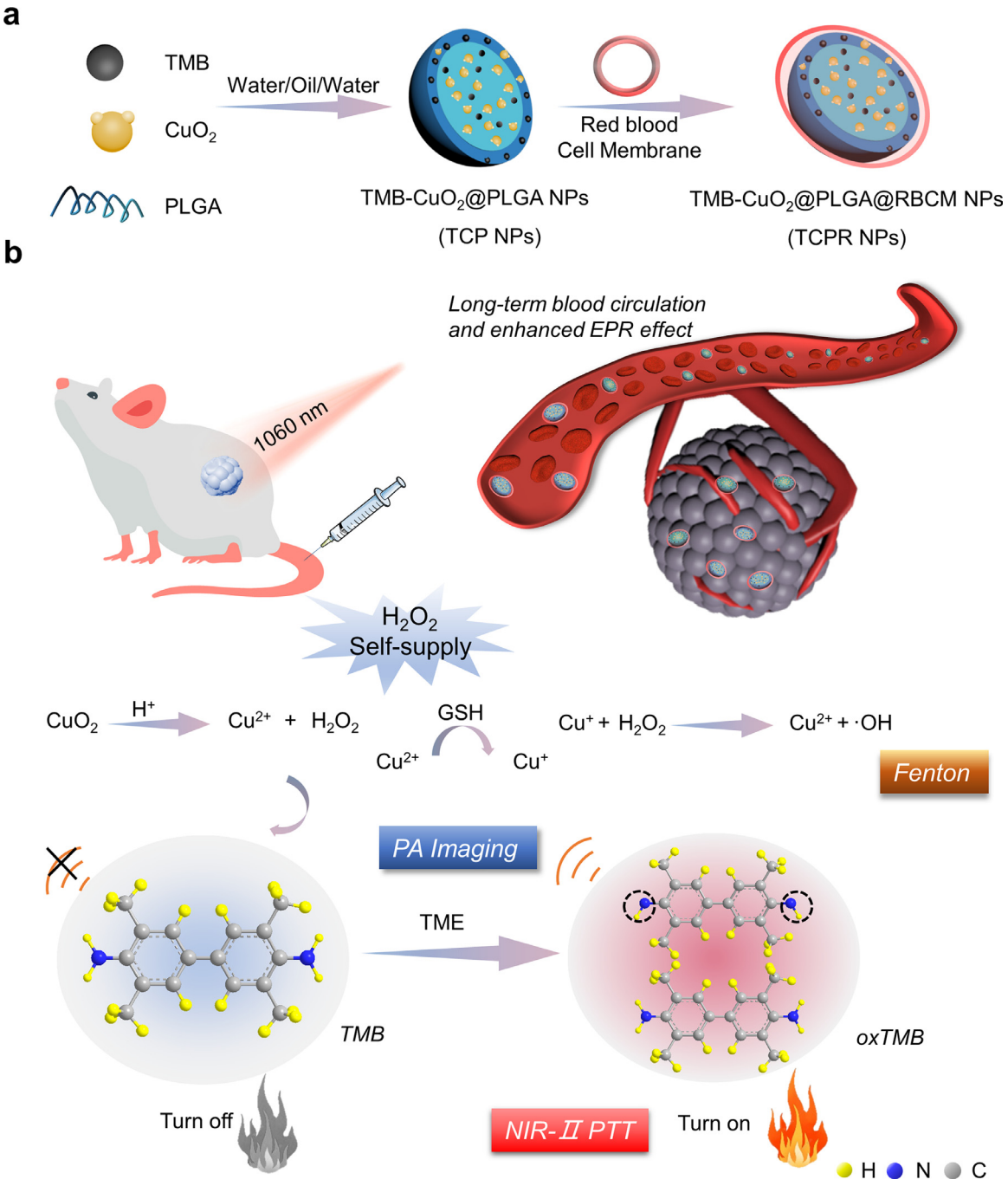

Scheme 1. (a, b) Schematic illustration of the synthesis of 3,3′,5,5′-tetramethylbenzidine (TMB)-copper peroxide (CuO_2)@poly(lactic-co-glycolic acid) (PLGA)@red blood cell membrane (RBCM) (TCPR) nanoparticles (NPs) and the mechanism of H_2O_2-activated specific photothermal therapy (PTT) guided by second near-infrared (NIR-II) photoacoustic imaging (PAI).

2.6. *In vitro cytotoxicity assay*

Mouse breast cancer cells (4T1) and human-immortalized keratinocytes (HaCaTs) were cultured in a medium (Roswell Park Memorial Institute-1640 for 4T1 and Dulbecco's minimal essential medium for HaCaTs purcharsed form Wuhan Servicebio technology Co. Ltd. containing 10% fetal bovine serum and 1% penicillin-streptomycin in the presence of 5% CO_2 at 37 ˚C). In regards to the cytotoxicity assay, a 96-well plate was inoculated with HaCaTs (2.0×10^4 cells per well), and the cells were incubated with different concentrations of TCPR NPs in a 100 μL complete culture medium. After a 12-h incubation period, each well received 20 μL of 3-(4,5-cimethylthiazol-2-yl)-2,5-diphenyl tetrazolium bromide (5 mg mL^{-1}), and the plate was kept at 37 ˚C for additional four hours. DMSO (200 μL) was used to dissolve the formazan crystals in living cells, and the absorbance of the purple-colored formazan/DMSO solution at 490 nm was measured using a microplate reader (MK3, Thermo Scientific, America) for the calculation of cell viability.

Finally, a 2,7-dichlorodi-hydrofluorescein diacetate probe was used to detect intracellular •OH. Dead cells emitted red fluorescence when stained with propidium iodide (PI), whereas live cells were stained with calcein acetoxymethyl ester (Calcein-AM), which emitted green fluorescence.

In a 6-well plate, 4T1 cells (5×10^6 cells per well) were seeded and incubated overnight. Different substances (PBS, TPR, TPR + NIR, TCPR,

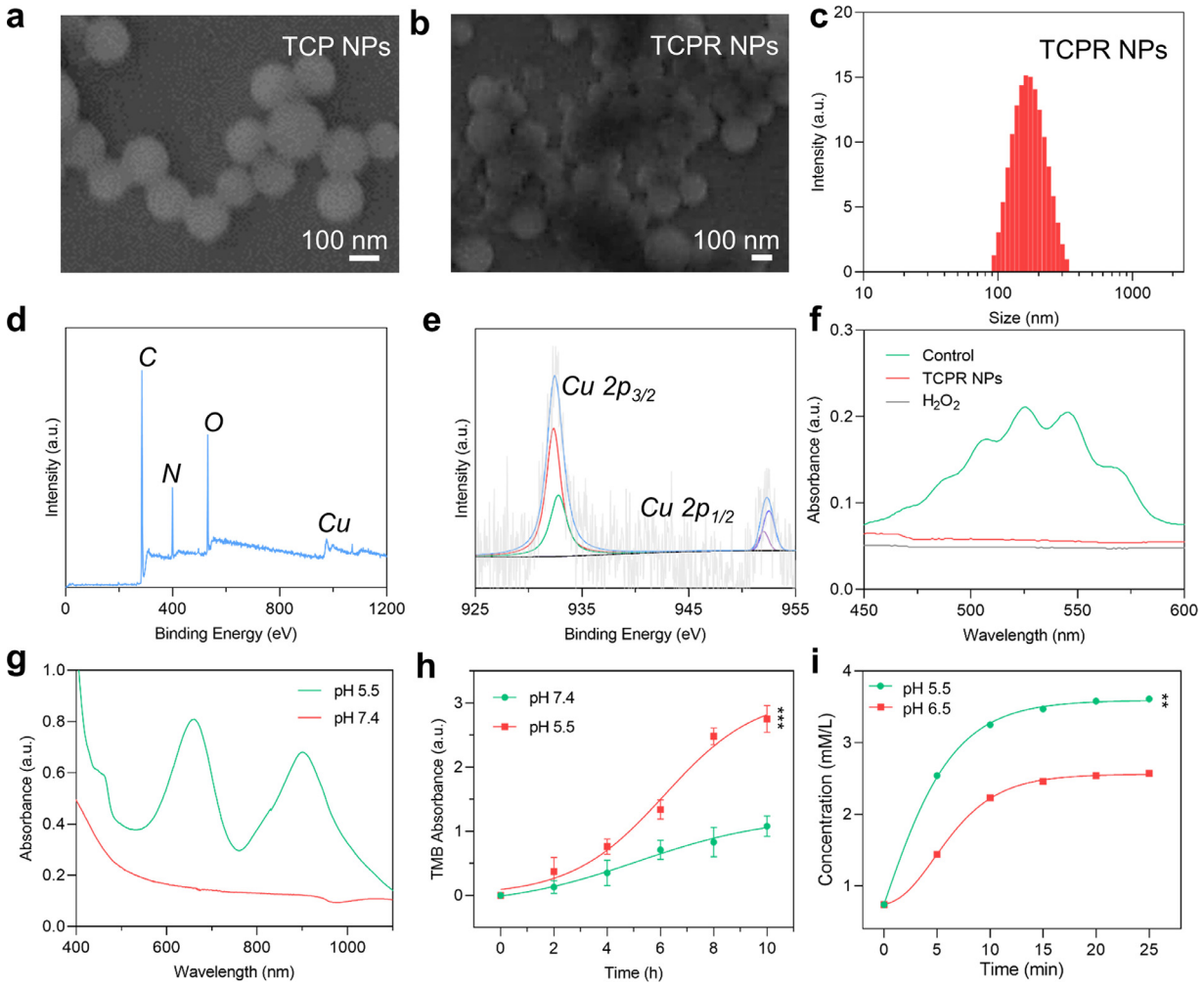

Fig. 1. (a,b) Scanning electron microscope (SEM) images of 3,3′,5,5′-tetramethylbenzidine (TMB)-copper peroxide (CuO_2)@poly(lactic-co-glycolic acid) (PLGA) (TCP) and TCP@red blood cell membrane (RBCM) (TCPR) nanoparticles (NPs). (c) Hydrodynamic size distribution of TCPR NP solution (polydispersity index: 0.258). (d) X-ray photoelectron spectroscopy (XPS) survey spectrum. (e) Cu 2p XPS spectra at high resolution. Ultraviolet (UV)–visible (Vis)–near-infrared (NIR) absorption spectra of (f) $KMnO_4$ incubated with PBS (Control), TCPR NPs, and H_2O_2 for detecting the generation of H_2O_2, (g) TCPR NPs at pH 5.5 and 7.4. (h) Absorbance of the released TMB at different time points under pH 5.5 and 7.4. (i) Concentration changes of H_2O_2 with time changes generated by TCPR NPs at pH 6.5 and 5.5 ($^{***}p < 0.001$, $^{**}p < 0.01$).

and TCPR + NIR) were added to each well at a concentration of 100 μg mL^{-1}. The laser irradiation group received 10 min of 1060 nm laser irradiation (1 W cm^{-2}) after a 4-h incubation, and the cells were cultured for another 8 h before conducting western blotting analysis.

2.7. NIR-II PA imaging

TCPR NP aqueous suspensions (25, 50, 75, and 100 μg mL^{-1}) were simultaneously injected into PA glass tubes, and the PA intensity of the samples under 1060 nm laser irradiation was subsequently determined.

To detect the *in vivo* PA signals at the tumor sites, 4T1 tumor-bearing mice were *i.v.* injected with 200 μL of TCPR NPs (500 μg mL^{-1}), and placed into the LOIS-3D machine to gather PA signals.

2.8. Animal models

The Yangzhou University Comparative Medicine Centre provided female mice (BALB/c, 5–6 weeks old), and 4T1 cells were inoculated subcutaneously in the right rear to build a local tumor model. All animal experiments were monitored and authorized by the School of Pharmaceutical Science, Nanjing Tech University. Female Balb/c mice were ordered from the Comparative Medicine Centre of Yangzhou University's animal ethics (permit number:SCXK (SU) 2017-0007).

2.9. In vivo assay

The 4T1 tumor-bearing mice were randomly distributed into five groups (n = 4) and *i.v.* injected with 100 μL of the following formulations when the tumor volume reached 100–120 mm^3: (1) control (PBS), (2) CuO_2 NPs, (3) TPR NPs + NIR, (4) TCPR NPs, and (5) TCPR NPs + NIR. The concentration of the NPs was 4 mg/kg. After administration for 8 h, 10 min of laser irradiation (0.5 W cm^{-2}, 1060 nm) was applied to the 4T1 tumor-bearing mice in groups (3) and (5), and tumor volumes and body weights were measured every two days.

2.10. Intratumoral dihydroethidium (DHE) staining and copper ion detection

While frozen sections of fresh tumors were stored at –20 °C, DHE could enter the cells and be oxidized by intracellular reactive oxygen species (ROS) to emit red fluorescence. The brighter the red fluorescence, the higher were the cellular ROS levels.

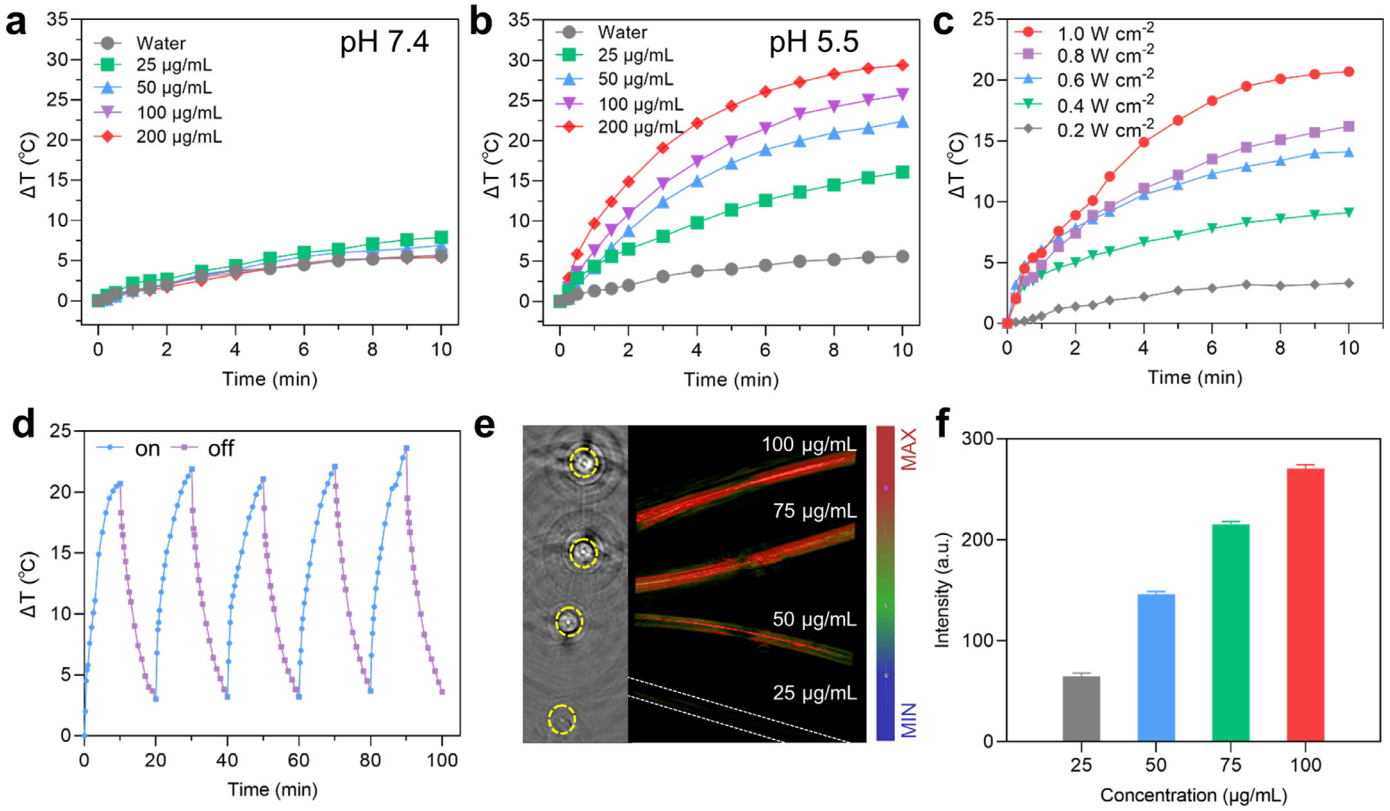

Fig. 2. (a,b) Quantitative temperature curve of TCPR NPs with different concentrations at pH 7.4 and 5.5 (1060 nm, 1 W cm^{-2}, 10 min). (c) Temperature variations of TCPR NPs (100 μg mL^{-1}) irradiated by 1060 nm laser at different power densities. (d) Photothermal stability of TCPR NPs exposed to laser irradiation (1060 nm, 1 W cm^{-2}) for 5 on/off cycles. (e) Photoacoustic (PA) images of TCPR NP suspensions at various concentrations (25–100 μg mL^{-1}). (f) Quantitative PA intensities corresponding to the PA signals in (e).

Tumor tissue sections were treated with ethanolic ruby acid and sodium acetate solutions to detect Cu ions, while excess rubric acid combined to form dark green-black rubric Cu salt precipitates.

2.11. In vivo histochemical analysis

The mice were sacrificed at the end of the treatment, and their spleen, liver, heart, kidney, lung, and tumor tissues were fixed with 4% paraformaldehyde (Wuhan Servicebio technology Co. Ltd.). Ki-67 and hematoxylin and eosin (*H&E*) were used to stain the tissues before examination under an optical microscope.

3. Results and discussion

The smart TME-triggered theranostic system is expected to remarkably improve the efficiency of tumor management and resultant patient outcomes. Hence, TME-responsive PTT is extremely beneficial to patients. As illustrated in Scheme 1, CuO_2 NPs (~12 nm) were first synthesized according to a previous study [29], and the crystal structure was confirmed by the XRD spectrum (Fig. S1). TCP NPs were fabricated by co-loading TMB and CuO_2 NPs into a water/oil/water (w/o/w) double emulsion formed by PLGA to realize NIR-II PAI-guided tumor-specific PTT. RBCM was employed to modify TCP NPs (TCPR NPs) via self-assembly to achieve long-term blood circulation.

As shown in Fig. 1a, the TCP NPs exhibited a regular homogeneous spherical shape, with an average diameter of 124 nm. The roughness of the surface of the TCPR NPs increased after surface modification with RBCM (Fig. 1b). In turn, the low zeta potential of TCPR NPs compared to that of TCP NPs further confirmed effective surface modification (Fig. S2). The hydrodynamic size distribution of TCPR NPs in water was ~125 nm (Fig. 1c), which is consistent with the SEM results. The atomic composition was confirmed by XPS (Fig. 1d and S3). The Cu $2p_{1/2}$ and Cu $2p_{3/2}$ peaks of the XPS Cu spectrum in Fig. 1e deconvoluted into their peak at 932.3 eV from Cu^+ and at 952.5 eV from Cu^{2+} [30]. $KMnO_4$ was chosen as the detection probe to investigate the H_2O_2 generation ability of the developed TCPR NPs, whose characteristic UV–Vis–NIR absorption peaks would dissolve due to H_2O_2 oxidation. As shown in Fig. 1f, five distinct $KMnO_4$ peaks were identified in the control group, but when $KMnO_4$ was treated with H_2O_2 or TCPR NPs, the characteristic absorption disappeared, indicating the H_2O_2 generating capability of TCPR NPs. The existence of Cu^+/Cu^{2+} redox couples together with the H_2O_2 generating capability of TCPR NPs verified the H_2O_2 self-supply property of TCPR NPs in an acidic environment ($CuO_2 + 2H^+ \rightarrow Cu^{2+} + H_2O_2$). Under acidic conditions, the Fenton-like reaction mediated by hydrolyzed Cu ions and endogenous/generated H_2O_2 produces •OH, further oxidizing TMB into oxTMB (Fig. S4). The absorption spectra of TCPR NPs were analyzed at pH 7.4 (to mimic normal tissue) and pH 5.5 (to mimic tumor tissue) to assess the selectivity of TCPR NPs for acidity. The characteristic oxTMB absorption spectrum showed that the release rate was faster at pH 5.5, within 10 h of the test, with the release amount corresponding to pH 5.5, which was nearly three times that at pH 7.4, confirming the specificity of TCPR in acidic environments (Fig. 1g). Furthermore, the release of TMB at pH 5.5 reached a maximum at 10 h, which was nearly 3-fold the release at pH condition of 7.4 (Fig. 1h). In addition, KI was used as the probe to detect self-supplied H_2O_2 at pH 5.5, and pH 6.5. At pH 5.5, the generation rate of H_2O_2 was significantly higher than that at pH 7.4, as shown in Fig. 1i. These results revealed that the recently obtained TCPR NPs possess the capability of H_2O_2 self-supplementary and specific release of TMB in an acidic environment, enabling self-enhanced and TME-activated PTT.

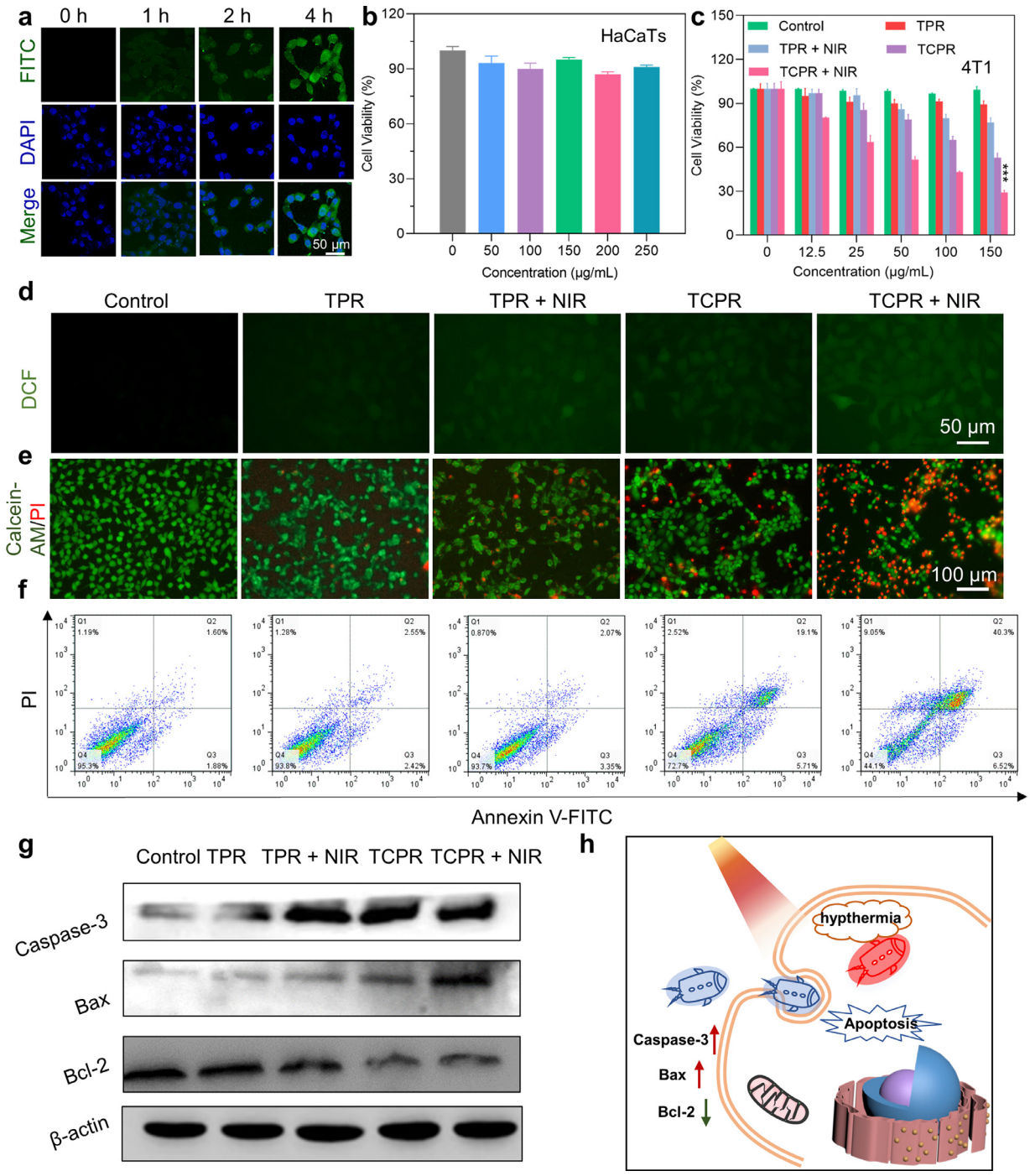

Fig. 3. (a) Cellular uptake and localization of fluorescein isothiocyanate (FITC)-labeled TCPR NPs (green fluorescence) at a concentration of 100 μg mL^{-1} at different time points. The cell nuclei were stained with 4′, 6-diamidino-2-phenylindole (DAPI). (b) Cell viability of human-immortalized keratinocytes (HaCaTs) incubated with TCPR NPs at various concentrations. (c) Viability of 4T1 cells cultured with NPs of TPR or TCPR at different concentrations with and without laser irradiation (10 min, 1 W cm^{-2}, 1060 nm). (d) Reactive oxygen species (ROS) staining for intracellular radical detection (incubated with NPs [50 μg mL^{-1}] for 8 h). (e) Live/dead staining of 4T1 cells after treatment (50 μg mL^{-1}) under laser irradiation (10 min, 1 W cm^{-2}, 1060 nm). (f) Annexin-V-FITC/propidium iodide (PI) flow cytometry assay. (g) Western blotting assay of caspase-3, B-cell lymphoma (Bcl)-2, and Bcl-2-associated X (Bax) protein expression. (h) Schematic illustration of cell apoptosis caused by TCPR NP-induced hypothermia (***$p < 0.001$).

Compared with the NIR-I biowindow (750–1000 nm), the NIR-II biowindow (1000–1350 nm) has very recently attracted more attention due to its higher maximum allowable exposure (MPE) to laser (e.g., 0.33 W cm^{-2} for 808 nm light, 1 W cm^{-2} for 1060 nm light), as well as its deeper tissue penetration depth. We further evaluated the photothermal performance of TCPR NPs under different conditions. As shown in Fig. 2a–c, TCPR NPs showed concentration-, pH-, and laser power density-dependent photothermal efficiency. Impressively, benefiting from the effective generation of H_2O_2 under acidic conditions (pH 5.5), the temperature of the TCPR NPs solution (100 μg mL^{-1}) increased by over 25 °C, which was significantly higher than that in the neutral pH condition. This again confirmed the selective oxidation of TMB by introducing CuO_2 NP and ensured tumor-specific PTT with minimal side effects to adjacent normal tissues (Fig. 2a and b). Under 1060 nm laser ir-

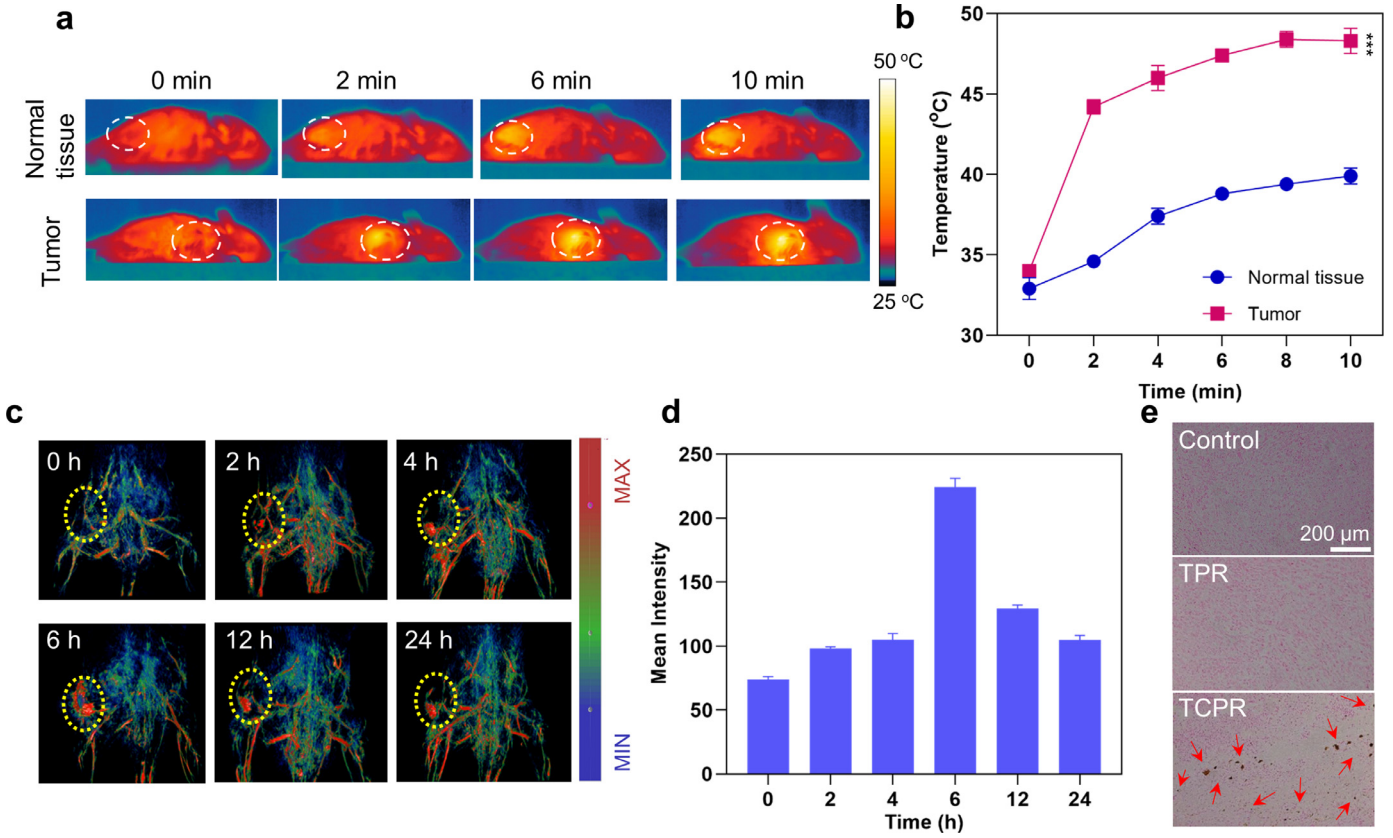

Fig. 4. (a) Photothermal pictures of the treatment with TCPR NPs (50 μg mL^{-1}, 200 μL), which were irradiated with 1060 nm laser (1 W cm^{-2}) at the tumor sites for 10 min. (b) Corresponding temperature change in (a). (c) Copper red acid staining of tumor tissues. (d) PA images of mice at various time points after the intravenous injection of TCPR NPs. (e) Corresponding PA signal intensities in (d) (***$p < 0.001$).

radiation, the TCPR NPs presented an excellent PCE efficiency ($\eta = 54\%$, Fig. S5) and outstanding photothermal stability (Fig. 2d) as a photothermal agent.

As expected, TCPR NPs at pH 5.5 showed desirable PAI performance and a concentration-dependent increase in PA signal (Fig. 2e and f), which revealed that TCPR NPs exhibit a TME-responsive photothermal effect and satisfactory PAI performance for directing and assessing the treatment process. Inspired by their superior physicochemical properties, the anticancer effects of the TCPR NPs were further tested at the cellular level. By incubating 4T1 cells with fluorescein isothiocyanate (FITC)-labeled TCPR NPs for different time intervals, we found that TCPR NPs were effectively endocytosed within 4 h and were distributed in both the nucleus and cytoplasm (Fig. 3a). TCPR NPs at concentration of 0-250 μg mL^{-1} exhibited no apparent toxicity to HaCaTs (Fig. 3b), whereas they were dose-dependently cytotoxic to 4T1 tumor cells, presumably because cancer cells have a relatively higher H_2O_2 level than normal cells. 4T1 cells were treated with nanoparticles of different formulations, with or without laser irradiation, to further investigate the anticancer mechanism of TCPR NPs. The relative survival rate of cancer cells treated with TPR nanoparticles (without CuO_2) did not decrease significantly during laser irradiation, as seen in Fig. 3c. Interestingly, when 4T1 cells were cultured with the TCPR NPs for 6 h, a large number (~40%) of cancer cells were killed, which could be due to the Fenton-like reaction of Cu ions with the self-supplied H_2O_2 and endogenous H_2O_2., which is demonstrated by the significantly increased ROS levels in the TCPR and TCPR + NIR groups (Fig. 3d).

To a certain extent, the laser promoted ROS production, and the relative cell viability in the TCPR NPs + NIR group decreased remarkably, indicating the highly efficient tumor-killing effect of this TCPR NP-based treatment, which could be attributed to the oxidation of TMB. Calcein-AM and PI were used to stain live and dead cells, respectively, to further confirm the treatment performance of TCPR NPs (Fig. 3e). Although the TPR, TPR + NIR, and TCPR groups exhibited limited lethality to 4T1 cells and most of them showed green fluorescence, significant red fluorescence was observed in the TCPR group, which indicated an effective anticancer effect triggered by the prominent synergistic effect of enhanced PTT. Flow cytometric analysis was used to quantify cell apoptosis and necrosis. As shown in Fig. 3f, the annexin V-FITC/PI double staining assay was used to examine apoptotic and necrotic cells. While almost no apoptotic or necrotic cells were observed when 4T1 cells were treated with TPR and TPR+NIR groups, 27.33% of apoptotic/necrotic cells were induced when treated with TCPR NPs alone, and 55.87% of apoptotic/necrotic cells in the TCPR group were observed. With the assistance of TME responsiveness and laser irradiation, TCPR NPs demonstrated excellent cytotoxicity in tumor cells and a favorable synergistic therapeutic effect. Additionally, as the key regulators of cell apoptosis and necrosis, the expression levels of the B-cell lymphoma (Bcl)-2 family (Bcl-2-associated X protein (Bax) and Bcl-2) and caspase family proteins (Caspase-3) in 4T1 cells after different treatments (PBS, TPR, TPR + NIR, TCPR, and TCPR + NIR) were analyzed by western blotting (Fig. 3g). Bcl-2 was downregulated, Bax was upregulated, and its value gradually decreased after the promotion of cell apoptosis, consistent with the upregulation of Caspase-3. As discussed above, the TCPR NPs self-supplied with H_2O_2 in cancer cells could activate TMB oxidization with Cu ions, which would induce a potent photothermal effect and kill cancer cells by activating the apoptotic/necrotic cascade (Fig. 3h).

Bioimaging provides information on lesions and monitors the spatiotemporal distribution of nanomedicines, thus enabling more precise phototherapy and reducing the potential damage to normal tissues. Here, we investigated the *in vivo* photothermal performance of TCPR

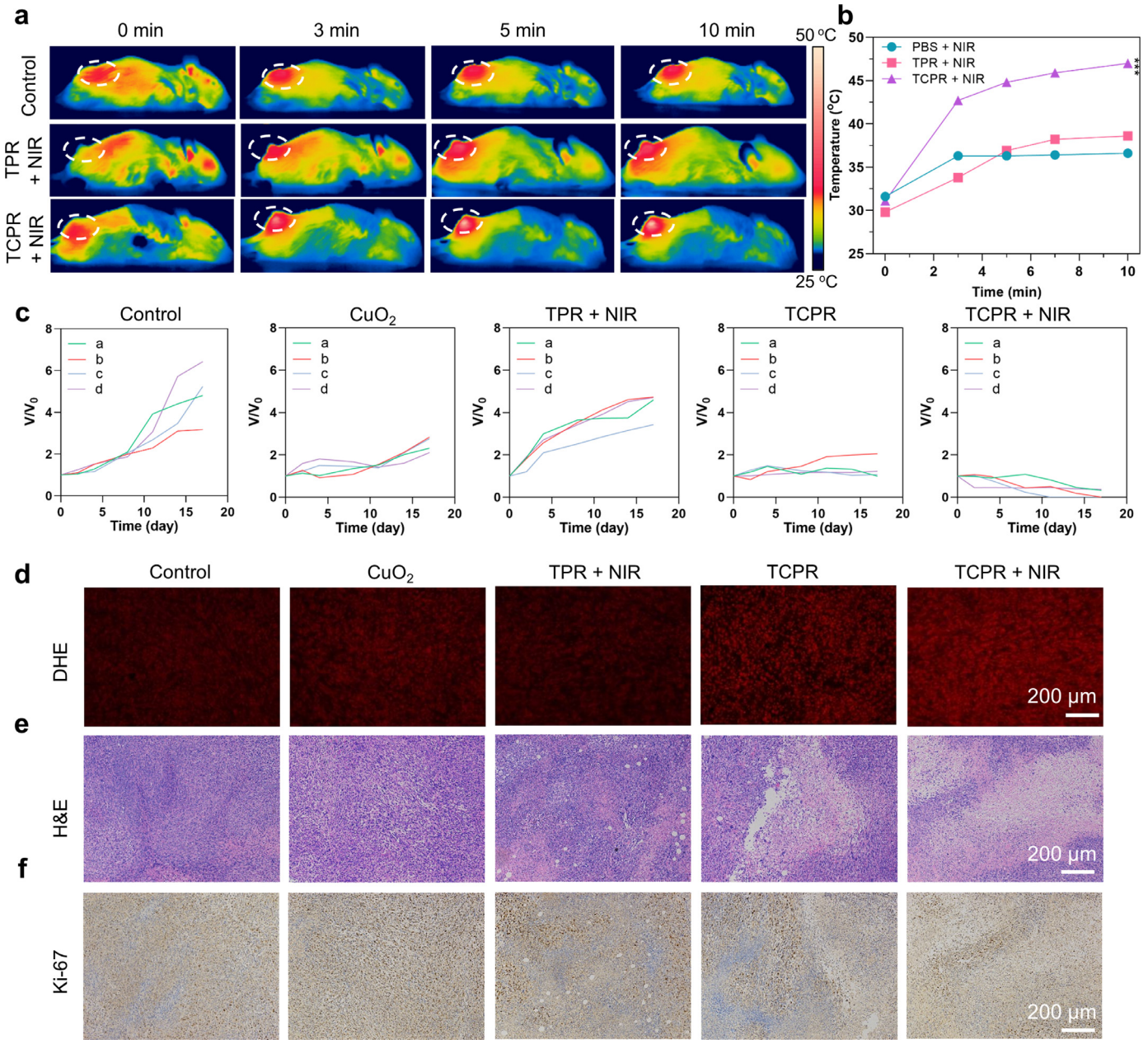

Fig. 5. (a) Photothermal pictures of mice treated under 1060 nm laser irradiation (1 W cm^{-2}) for different time points after being injected with TPR or TCPR NPs (200 μg mL^{-1}, 50 μL) and phosphate-buffered saline (PBS.) (b) Temperature changes in mice tumor sites corresponding to (a). (c) Variation in relative tumor volume after different treatments. (d–f) Dihydroethidium (DHE; red fluorescent signal indicates ROS concentration), hematoxylin and eosin (H&E), and Ki-67 staining of tumors with various treatments (***$p < 0.001$).

NPs using the absorption of TCPR in the NIR-II range, in which T was injected subcutaneously into normal tissue and intratumorally (Fig. 4a and b). Notably, while the temperature in normal tissue only increased to 39.9 °C, the tumor temperature increased to 48.4 °C after 10 min of laser irradiation (1060 nm, 1 W cm^{-2}), indicating that TCPR NPs could be triggered explicitly by the TME while maintaining stealth in normal tissues. As the TME-triggered imaging ability of the TCPR NPs could be used to guide *in vivo* therapy, PAI was further used to assess the *in vivo* performance of TCPR NPs after *i.v.* injection. As shown in Fig. 4d and e, the PA signal of the tumor site appeared 2 h post-injection and gradually increased over time. The maximum tumor accumulation of the NPs occurred at 6 h, after which the PA signal intensity was gradually attenuated. Copper red acid staining was conducted to confirm the presence of TCPR NPs in the tumor. In turn, the copper salt deposition was dark green and black, and the nuclei were red. In the comparison between the control and TPR groups, copper salt deposition was observed in the TCPR group (Fig. 4c), which confirmed the apparent tumor uptake of the TCPR nanoparticles.

Mice were randomly distributed into five groups and injected with different formulations through the tail vein (CuO_2, TPR + NIR, TCPR, TCPR + NIR, and control, $n = 4$) to assess the *in vivo* antitumor performance of TCPR NPs-based PTT. The temperature of the tumor injected with the TCPR NPs increased to 47.2 °C 6 h later, with 10 min of laser irradiation, while the control group and TPR + NIR group only increased to approximately 36 °C, which confirmed the photothermal effect (Fig. 5a and b).

Under laser irradiation, the reaction between endogenous H_2O_2 and TPR NPs suppressed tumor growth, even in the absence of CuO_2 NPs.

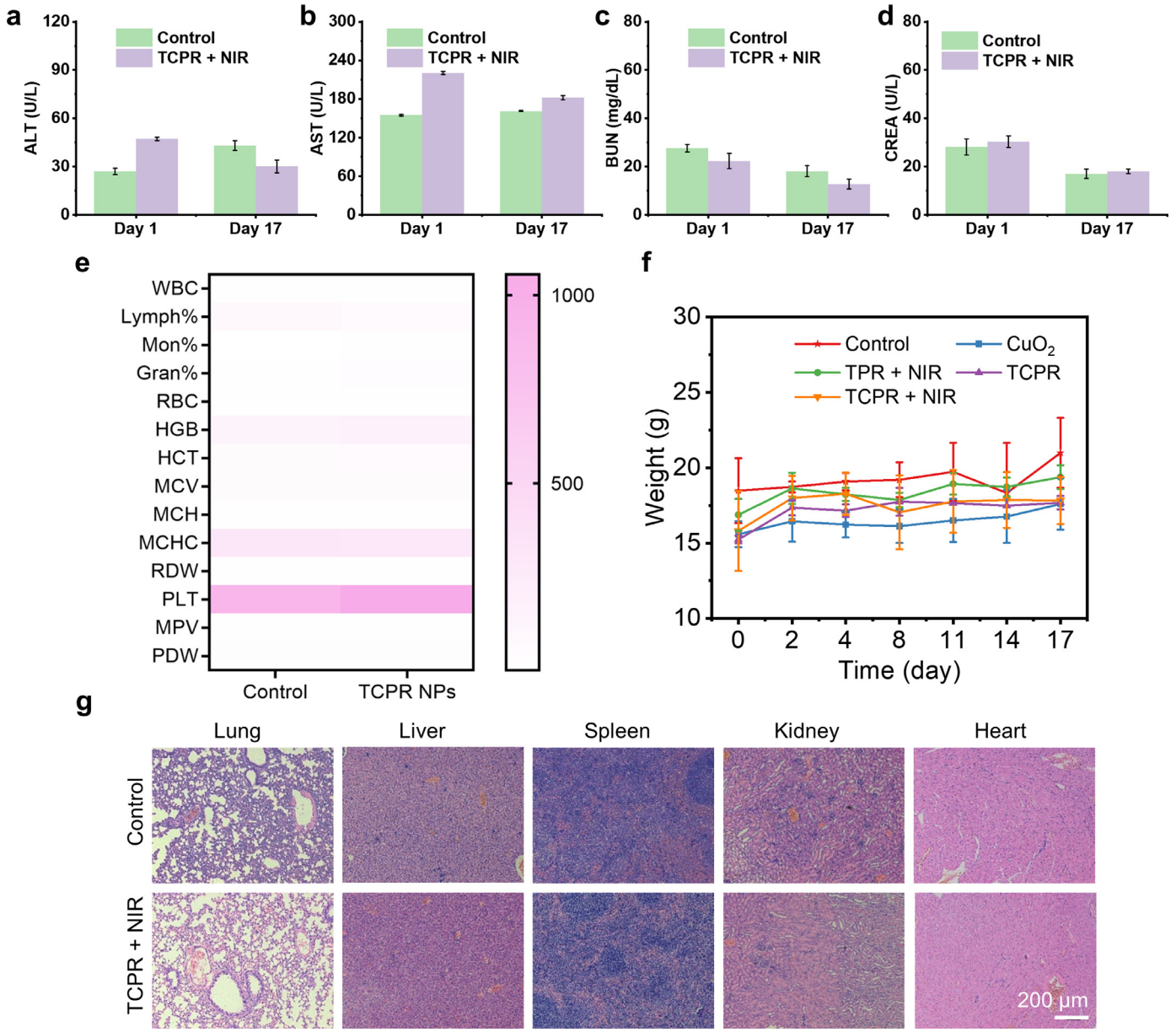

Fig. 6. (a–d) Alanine aminotransferase (ALT), creatinine (CREA), blood urea nitrogen (BUN), and aspartate aminotransferase (AST) levels in mice after receiving TCPR NPs via an intravenous (*i.v.*) injection. (e) Analysis of the complete blood panel of mice after *i.v.* injection of TCPR NPs, including white blood cells (WBCs), hematocrit (HCT), red blood cell distribution width (RDW), platelet distribution width (PDW), hemoglobin (HGB), mean corpuscular hemoglobin (MCH), platelets (PLTs), red blood cells (RBCs), mean corpuscular volume (MCV), mean corpuscular hemoglobin concentration (MCHC), mean platelet volume (MPV), lymphocyte (Lymph%), monocyte (Mon%), and granulocyte (Gran%). (f) The body weights of mice fluctuate during different treatments. (g) H&E staining of major organs in the control and TCPR + NIR groups.

The growth of the tumors treated with CuO_2 and TCPR nanoparticles exhibited some inhibition, which might be due to the chemodynamic effect induced by the hydrolyzed Cu ions with endogenous and/or self-generated H_2O_2. On the other hand, the TCPR-NIR group showed significantly suppressed tumor growth (~100% reduction in tumor volume compared to the control) after 10 min of laser irradiation, demonstrating the excellent therapeutic efficacy of TCPR NPs due to the self-supplied H_2O_2 and activated PTT (Fig. 5c and S6). Intratumoral ROS levels were determined by DHE staining (Fig. 5d). Compared to the other groups, TCPR NP treatment resulted in higher ROS levels in tumors, which were further elevated by laser irradiation-induced hyperthermia. H&E staining demonstrated apoptosis and necrosis of the tumor cells caused by PTT (Fig. 5e). The most severe damage was observed in the TCPR and TCPR + NIR groups. Furthermore, the Ki-67 (brown staining indicates cell proliferation) immunohistochemistry assay inhibited tumor cell proliferation (Fig. 5f), which showed the high antitumor efficiency of TME-responsive therapy based on TCPR NPs.

The long-term biosafety of TCPR NPs was further assessed via complete blood panel and blood biochemistry analyses, with all experimental groups maintaining normal levels of critical functional markers, such as alanine aminotransferase, aspartate aminotransferase, blood urea nitrogen, and creatinine, in the blood. The levels of aminotransferase in the tested groups did not change, which demonstrated that TCPR NPs were kidney- and liver-compatible (Fig. 6a–d). The evaluated fourteen common indexes for routine blood analysis were within the normal ranges, indicating the negligible blood toxicity of TCPR NPs for 17 days (Fig. 6e). Furthermore, the weights of the mice also showed no abnormal changes (Fig. 6f), indicating negligible systematic toxicity of the

treatment. Moreover, histological examination of the major organs of mice injected with PBS (as control) and TCPR NPs was performed to assess the potential toxicity (Fig. 6g), with no pathogenic abnormalities or inflammation observed in both groups. Collectively, these findings demonstrate the *in vivo* biocompatibility of TCPR NPs, paving the way for their future use as theranostic agents.

4. Conclusion

In conclusion, an activatable theranostic nanoreactor was developed for TME-triggered NIR-II PTT under PAI guidance. The obtained TCPR NPs, with their rational design, showed impressive on–off switchability for cancer-specific therapy and outstanding pH-responsive activities to generate H_2O_2 and Cu ions, which further resulted in the generation of •OH via a Fenton-like reaction and oxidized TMB, turning on the photothermal effect via the generation of oxTMB. TCPR NPs, which also benefited from the camouflage of RBCM, achieved long-term blood circulation and successfully accumulated in tumor tissues via the EPR effect. Moreover, theranostic TCPR NRs could be specifically activated at the tumor site to achieve high-efficiency PTT under 1060 nm laser irradiation without harming the normal tissues. Therefore, use of activatable TCPR NRs has proven to be a feasible approach for tumor-specific imaging and treatment with minimal side effects.

Declaration of competing interest

The authors declare that they have no conflicts of interest in this work.

Acknowledgments

This work was supported by the National Natural Science Foundation of China (62120106002, 51803091, 61935004, 22175089), Jiangsu Province Policy Guidance Plan (BZ2019014), Jiangsu Provincial key research and development plan (BE2021711), Natural Science Foundation of Shandong Province (ZR2020KB018), Taishan scholars construction special fund of Shandong Province, Natural Science Foundation of Ningbo (202003N40448), and the Jiangsu postgraduate research innovation program (KYCX21_1103).

Supplementary materials

Supplementary material associated with this article can be found, in the online version, at doi:10.1016/j.fmre.2022.04.021.

References

[1] R. Kumar, W.S. Shin, K. Sunwoo, et al., Small conjugate-based theranostic agents: an encouraging approach for cancer therapy, Chem. Soc. Rev. 44 (2015) 6670–6683.
[2] J. Xing, Q. Gong, O.U. Akakuru, et al., Research advances in integrated theranostic probes for tumor fluorescence visualization and treatment, Nanoscale 12 (2020) 24311–24330.
[3] N. Yan, X. Wang, L. Lin, et al., Gold nanorods electrostatically binding nucleic acid probe for *in vivo* microRNA amplified detection and photoacoustic imaging-guided photothermal therapy, Adv. Funct. Mater. 28 (2018) 1800490.
[4] X. Zhao, C.X. Yang, L.G. Chen, et al., Dual-stimuli responsive and reversibly activatable theranostic nanoprobe for precision tumor-targeting and fluorescence-guided photothermal therapy, Nat. Commun. 8 (2017) 14998.
[5] M. Wu, H. Zhang, C. Tie, et al., MR imaging tracking of inflammation-activatable engineered neutrophils for targeted therapy of surgically treated glioma, Nat. Commun. 9 (2018) 4777.
[6] G. Yu, S. Yu, M.L. Saha, et al., A discrete organoplatinum(II) metallacage as a multimodality theranostic platform for cancer photochemotherapy, Nat. Commun. 9 (2018) 4335.
[7] F. Gong, N. Yang, X. Wang, et al., Tumor microenvironment-responsive intelligent nanoplatforms for cancer theranostics, Nano Today 32 (2020) 100851.
[8] L. Zhang, Z. Wang, Y. Zhang, et al., Erythrocyte membrane cloaked metal–organic framework nanoparticle as biomimetic nanoreactor for starvation-activated colon cancer therapy, ACS Nano 12 (2018) 10201–10211.
[9] C. Xie, X. Zhen, Y. Lyu, et al., Nanoparticle regrowth enhances photoacoustic signals of semiconducting macromolecular probe for *in vivo* imaging, Adv. Mater. 29 (2017) 1703693.
[10] D. Chen, Y. Tang, J. Zhu, et al., Photothermal-pH-hypoxia responsive multifunctional nanoplatform for cancer photo-chemo therapy with negligible skin phototoxicity, Biomaterials 221 (2019) 119422.
[11] S. Bakthavatsalam, M.L. Sleeper, A. Dharani, et al., Leveraging γ-glutamyl transferase to direct cytotoxicity of copper dithiocarbamates against prostate cancer cells, Angew. Chem. Int. Ed. 57 (2018) 12780–12784.
[12] B. Shi, Q. Yan, J. Tang, et al., Hydrogen sulfide-activatable second near-infrared fluorescent nanoassemblies for targeted photothermal cancer therapy, Nano Lett. 18 (2018) 6411–6416.
[13] D. Chen, Q. Tang, J. Zou, et al., pH-responsive PEG–doxorubicin-encapsulated Aza–BODIPY nanotheranostic agent for imaging-guided synergistic cancer therapy, Adv. Healthc. Mater. 7 (2018) 1701272.
[14] Y. Wang, X. Huang, Y. Tang, et al., A light-induced nitric oxide controllable release nano-platform based on diketopyrrolopyrrole derivatives for pH-responsive photodynamic/photothermal synergistic cancer therapy, Chem. Sci. 9 (2018) 8103–8109.
[15] J. Zou, P. Wang, Y. Wang, et al., Penetration depth tunable BODIPY derivatives for pH triggered enhanced photothermal/photodynamic synergistic therapy, Chem. Sci. 10 (2018) 268–276.
[16] K. Fan, J. Xi, L. Fan, et al., *In vivo* guiding nitrogen-doped carbon nanozyme for tumor catalytic therapy, Nat. Commun. 9 (2018) 1440.
[17] L. Gao, K. Fan, X. Yan, Iron oxide nanozyme: a multifunctional enzyme mimetic for biomedical applications, Theranostics 7 (2017) 3207–3227.
[18] J. Golchin, K. Golchin, N. Alidadian, et al., Nanozyme applications in biology and medicine: an overview, Artif. Cells Nanomed. Biotechnol. 45 (2017) 1069–1076.
[19] C. Cao, N. Yang, H. Dai, et al., Recent advances in phase change material based nanoplatforms for cancer therapy, Nanoscale Adv. 3 (2021) 106–122.
[20] N. Yang, W. Xiao, X. Song, et al., Recent advances in tumor microenvironment hydrogen peroxide-responsive materials for cancer photodynamic therapy, Nano-Micro Lett. 12 (2020) 15.
[21] W.K. Ong, X. Yao, D. Jana, et al., Efficient production of reactive oxygen species from Fe_3O_4/ZnPC coloaded nanoreactor for cancer therapeutics *in vivo*, Small Struct. 1 (2020) 2000065.
[22] H.S. Jung, P. Verwilst, A. Sharma, et al., Organic molecule-based photothermal agents: an expanding photothermal therapy universe, Chem. Soc. Rev. 47 (2018) 2280–2297.
[23] Y. Cai, Z. Wei, C. Song, et al., Optical nano-agents in the second near-infrared window for biomedical applications, Chem. Soc. Rev. 48 (2019) 22–37.
[24] X. Ge, Q. Fu, L. Bai, et al., Photoacoustic imaging and photothermal therapy in the second near-infrared window, New J. Chem. 43 (2019) 8835–8851.
[25] Y. Lyu, J. Li, K. Pu, Second near-infrared absorbing agents for photoacoustic imaging and photothermal therapy, Small Methods 3 (2019) 1900553.
[26] X.Q. Zhang, X. Chen, X.B. Cheng, et al., Highly stable lithium metal batteries enabled by regulating the solvation of lithium ions in nonaqueous electrolytes, Angew. Chem. Int. Ed. 57 (2018) 5301–5305.
[27] X. Ding, C.H. Liow, M. Zhang, et al., Surface plasmon resonance enhanced light absorption and photothermal therapy in the second near-infrared window, J. Am. Chem. Soc. 136 (2014) 15684–15693.
[28] Y. Liu, W. Zhen, Y. Wang, et al., One-dimensional Fe2P acts as a Fenton agent in response to NIR-II light and ultrasound for deep tumor synergetic theranostics, Angew. Chem. Int. Ed. 58 (2019) 2407–2412.
[29] L.S. Lin, T. Huang, J. Song, et al., Synthesis of copper peroxide nanodots for H_2O_2 self-supplying chemodynamic therapy, J. Am. Chem. Soc. 141 (2019) 9937–9945.
[30] N. Karikalan, R. Karthik, S.M. Chen, et al., Sonochemical synthesis of sulfur doped reduced graphene oxide supported CuS nanoparticles for the non-enzymatic glucose sensor applications, Sci. Rep. 7 (2017) 2494.

Nan Yang is assiduously studying for a doctoral degree in the Institute of Advanced Materials, Nanjing Tech University (Nanjing Tech), Nanjing 211800, China, supervised by Prof. Xiaochen Dong. Her current research focuses on the development of functional nanomaterials with good biocompatibility and innovative strategies for designing tumor microenvironment-responsive.

Xiaochen Dong (BRID: 09638.00.66037) obtained his Ph.D. degree from Zhejiang University. Then he joined the School of Materials Science and Engineering at Nanyang Technological University as a postdoctoral. In 2012, he joined the Institute of Advanced Materials, Nanjing Tech University as a Full Professor. He has published more than 200 papers, including Adv. Mater., ACS Nano, etc. The current research involves biophotonics and bioelectronics, flexible electronics.